Considerations for analysis of endothelial shear stress and strain in FSI models of atherosclerosis

Miten Patel [b,g,1], Fotios Savvopoulos [a,b,g,1], Caleb C. Berggren [c], Lydia Aslanidou [d], Lucas H. Timmins [e,f], Ranil de Silva [b], Ryan M. Pedrigi [c], Rob Krams [g,*]

[a] Bioengineering, Imperial College, UK
[b] NHLI, Imperial College, UK
[c] Mechanical & Materials Engineering, University of Nebraska-Lincoln, USA
[d] Institute of Bioengineering, Ecole Polytechnique Fédérale de Lausanne, Switzerland
[e] Biomedical Engineering, University of Utah, USA
[f] Scientific Computing and Imaging Institute, University of Utah, USA
[g] Queen Mary University, School for Material Sciences and Engineering, UK

ARTICLE INFO

ABSTRACT

Atherosclerosis is a lipid driven chronic inflammatory disease that is characterized by the formation of plaques at predilection sites. These predilection sites (side branches, curved segments, and bifurcations) have often been associated with disturbed shear stress profiles. However, in addition to shear stress, endothelial cells also experience artery wall strain that could contribute to atherosclerosis progression. Herein, we describe a method to accurately obtain these shear stress and strain profiles.

We developed a fluid–structure interaction (FSI) framework for modelling arteries within a commercially available package (Abaqus, version 6.12) that included known prestresses (circumferential, axial and pressure associated). In addition, we co-registered 3D histology to a micro-CT-derived 3D reconstruction of an atherosclerotic carotid artery from a cholesterol-fed ApoE$^{-/-}$ mouse to include the spatial distribution of lipids within a subject-specific model. The FSI model also incorporated a nonlinear hyperelastic material model with regionally-varying properties that distinguished between healthy vessel wall and plaque.

FSI predicted a lower shear stress than CFD ($\sim-12\%$), but further decreases in plaque regions with softer properties ($\sim-24\%$) were dependent on the approach used to implement the prestresses in the artery wall. When implemented with our new hybrid approach (zero prestresses in regions of lipid deposition), there was significant heterogeneity in endothelial shear stress in the atherosclerotic artery due to variations in stiffness and, in turn, wall strain.

In conclusion, when obtaining endothelial shear stress and strain in diseased arteries, a careful consideration of prestresses is necessary. This paper offers a way to implement them.

1. Introduction

Atherosclerosis is a chronic, lipid-driven inflammatory disease that progresses from simple to advanced plaques composed of a soft, lipid-rich necrotic core covered by a thin cap. Although it is a multifactorial disease, plaques tend to localize in regions of the vasculature with high curvature, side branches or bifurcations. The endothelium of these vessel regions often experiences disturbed blood flow and decades of research have demonstrated a correlation between arterial regions and locally disturbed flow and atherosclerosis (Morbiducci et al., 2016; Yurdagul et al., 2016). Recent studies, including ours, have demonstrated a causal, not just correlative, relationship between disturbed flow and the development of advanced atherosclerotic plaques (Cheng et al., 2006; Pedrigi et al., 2016, 2015).

While blood flow-derived shear stress on the endothelium has been used in research for the development of metrics to predict atherosclerosis progression and plaque composition, the performance of these metrics in patients is still debated (Stone et al., 2018). In addition to
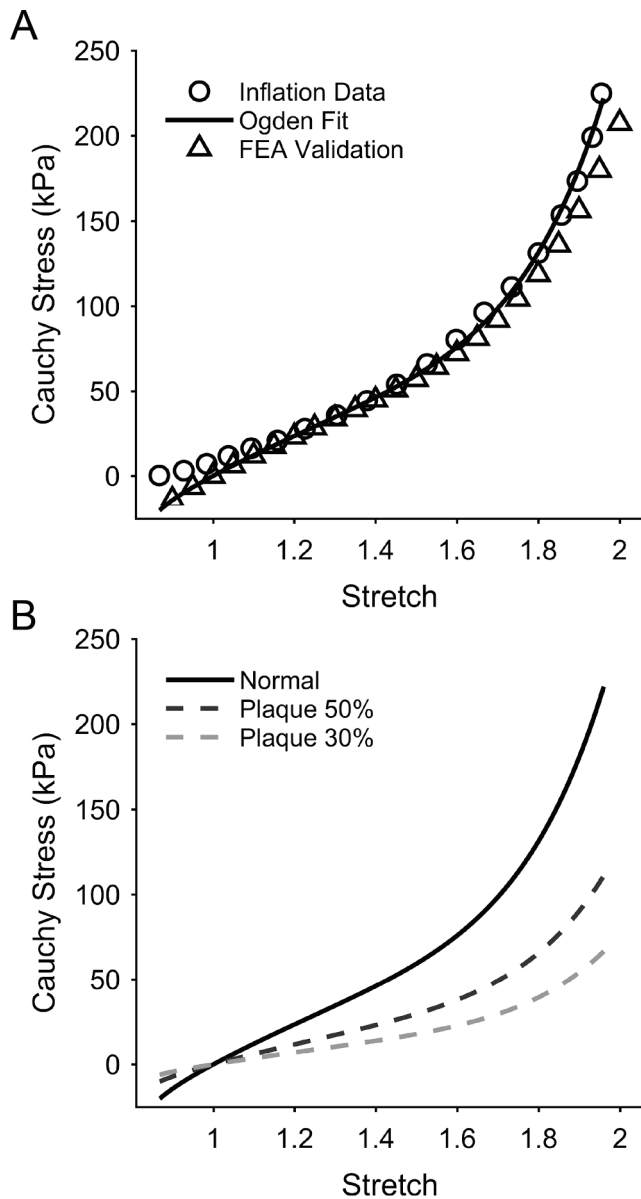

Fig. 1. Mechanical behaviour of the normal and atherosclerotic carotid artery models. (A) Comparison of the mechanical behaviour from empirical inflation data (Eberth et al., 2009), the fit of the Ogden hyperelastic model, and simulated equibiaxial testing using FEA. (B) The Ogden model used for the normal artery wall (solid line) and regions of lipid deposition (dashed lines), wherein the stiffness of the latter was reduced to 50% and 30% of the normal stiffness, respectively, based on the degree of lipid staining.

time-dependent shear stress, endothelial cells also experience pulsatile, blood pressure-induced artery wall stress and strain (Kobielarz et al., 2020; Pedrigi et al., 2014, 2017). The role of endothelial strain in atherogenesis has been far less studied than shear stress, but previous work by us and others have shown that disturbed strain profiles activate pro-atherogenic pathways similar to shear stress (Chester et al., 2014; Kwak et al., 2014; Liu et al., 2013; Pedrigi et al., 2017; Peters et al., 2015). The accumulation of lipids strongly enhances the heterogeneity of the mechanical environment in the plaque-affected areas. Thus, use of modelling techniques that allow elucidation of the highly heterogeneous mechanical environment of atherosclerotic plaques with stiff collagen-rich areas juxtaposed to soft lipid-rich zones (Alberts-Grill et al., 2013; Chistiakov et al., 2015; Krams et al., 2005; Tian et al., 2014; Trogan et al., 2002), may shed light on the still largely unknown mechanobio-logical effects of complex strain fields on endothelial cells and improve
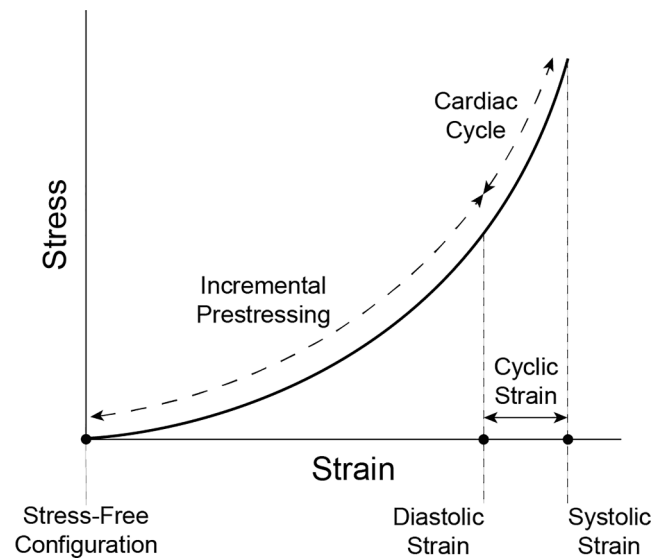

Fig. 2. Illustration of the nonlinear mechanical behaviour of the mouse carotid artery from the stress-free configuration. Diagram shows the strain due to the different prestresses and the additional strain induced by the cardiac cycle, called cyclic strain.

metrics seeking to predict atherosclerosis progression.

Accordingly, this paper describes the development of a fluid–structure interaction (FSI) model from *in vivo* micro-CT imaging of the carotid arteries of an ApoE$^{-/-}$ mouse that incorporates most mechanical complexities of the blood and diseased artery wall. These complexities include: circumferential residual stress, axial prestress, circumferential prestress due to diastolic blood pressure (Fung, 1991; Taber, 1995), and a nonlinear hyperelastic material model that has regionally-varying stiffness determined by co-registered histology to discriminate between healthy vessel wall and regions of lipid deposition in athero-sclerotic plaques. In line with previous reports, we demonstrate that a distensible artery wall in FSI causes a substantial reduction to the pre-dicted wall shear stress compared to the use of a rigid wall in CFD (Trachet et al., 2015). In addition, there was a further reduction in wall shear stress within the plaque regions which was dependent on the approach used to implement the residual stress and prestresses in the artery wall.

2. Methods

2.1. Animals, surgery, imaging, histology and mesh generation

The model geometry, inlet velocity boundary condition and co-registered 3D histology used to develop the FSI model were based upon a subset (1 female ApoE$^{-/-}$ mouse) of the data available from a prior study (Pedrigi et al., 2016) (Fig. S1, Appendix A). This mouse, aged 11 weeks, was placed on a high-fat diet and two weeks later instru-mented with a blood flow-modifying tapering cuff around the left ca-rotid artery, as previously described (Cheng et al., 2006; Pedrigi et al., 2016). The right carotid artery served as an un-instrumented control. The mouse was injected with a metal-based nanoparticle contrast agent and scanned using an ultra-high precision micro-computed tomography (micro-CT) system (isotropic resolution of 39.6 µm; Siemens Inveon scanner), which included respiratory and cardiac gating, nine weeks after placement of the cuff to reconstruct the *in vivo* geometry of both the diseased and control arteries. Pulsed Doppler ultrasound measurements (Vevo 770 Visualsonics) of blood velocity at the inlet of each carotid artery were conducted 1–3 days after micro-CT imaging. The mouse was then euthanized, its vessels perfusion-fixed, both carotid arteries were dissected, snap-frozen in OCT and stored for histological processing.
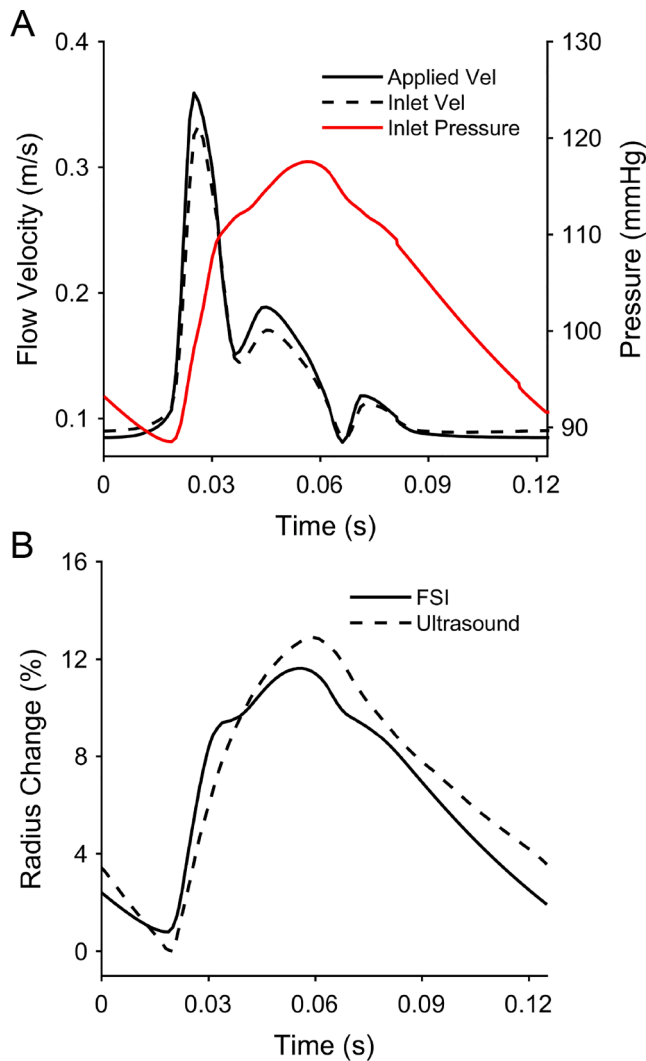
Fig. 3. Comparison of simulation model boundary conditions and radial displacement versus *in vivo* measurements from ultrasound. (A) Inlet flow velocity closely matched the flow velocity prescribed at the start of the inlet extension with the pressure waveform generated via the outlet boundary model. (B) FSI artery dilatation (% change in radius) compares well to empirical measurements from ultrasound.

Tissue blocks were serially sectioned from the aortic arch to the carotid bifurcation, stained using oil red O (ORO) to identify plaque structure and lipid concentration, and imaged at 10x magnification.

Three-dimensional (3D) reconstructions of the lumen of the control and instrumented vessels were obtained from the back-projected micro-CT slices using a level-set segmentation method. Reconstruction of the vessel wall was obtained through a multistep process that involved co-registration of histology to the reconstructed vessel lumen (Segers et al., 2007). Briefly, the imaged histological sections were manually segmented (to identify the lumen, internal elastic lamina, and external elastic lamina), binarized using a threshold to identify lipid staining, and digitized in Clemex. These data were then imported into a custom MATLAB program that performed co-registration using the aortic arch, cuff region, and carotid bifurcation of the lumen as landmarks, which corrected for longitudinal shrinkage. Circumferential co-registration was done by placing an ink line on the outer curvature of the artery prior to isolation. Radial co-registration of histology was performed by warping the histology on the 3D reconstructed vessel lumen assuming isotropic shrinkage of the vessel wall. Wall thickness and lipid stain information from histology was then interpolated over the nodes of the reconstructed lumen. The control vessel was also reconstructed from micro-CT, but only simulated using a nominal thickness.

The meshing of the vessel lumen uses the lumen wall outline STL reconstructed from micro-CT. The mesh was created with linear hexahedral elements with a boundary layer mesh of 10% of the radius consisting of three layers with growth rate of 1.2. The vessel wall was meshed using a custom program in MATLAB, which also employed hexahedral elements. The nodes on the luminal surface were located to coincide with the nodes on the inner wall of the artery mesh to improve the FSI interaction efficiency. Convergence tests were performed to identify a final mesh density that demonstrated less than 1% error for both stress/strain in the wall and shear stress in the lumen.

2.2. Material properties

Mechanical properties for the artery wall were obtained from previously reported mechanical behaviour data from inflation testing of wild type mouse carotid arteries (Eberth et al., 2009). These data demonstrated a nonlinear elastic mechanical behaviour over finite strains that was modelled using the isotropic Ogden hyper-elastic constitutive relation. The Ogden strain energy function, W, is given by

$$W = \sum_{i=1}^{N} \frac{2\mu_i}{\alpha_i^2} \left(\lambda_1^{\alpha_i} + \lambda_2^{\alpha_i} + \lambda_3^{\alpha_i} - 3 \right) \tag{1}$$

where μ, α, and N are material parameters and λ_i are the principal stretches in the circumferential, axial, and radial directions. These material parameters were identified for the non-diseased portions of the artery wall through a nonlinear regression to previously reported inflation data (Cauchy stress versus stretch) for the wild type mouse carotid artery (Eberth et al., 2009); best-fit parameters were: $\mu_1 = 20.56$, $\alpha_1 = 1e\text{-}5$, $\mu_2 = 0.785$, $\alpha_2 = 10.10$, which demonstrated an excellent fit to the data (Fig. 1A). In plaque regions with lipid uptake, the same Ogden model was used and the μ_i parameters were scaled based on the ratio of previously reported stiffness values of lipid-rich areas of plaque to normal wall (Fig. 1B) (Tracqui et al., 2011). Lipid stain intensities from the digitized and co-registered histology were separated into two different diseased material types based on the degree of staining. The stiffness of each material, assessed for each element of the model, was reduced to 50% and 30% of normal (i.e., no staining), respectively, based on the degree of lipid staining. The normal and diseased components of the vessel wall were given a density of 1050 kg/m^3 and Poisson's ratio of 0.495 (nearly incompressible, which is appropriate because the artery wall is 70% to 80% water by weight and exhibits nearly isochoric motions under physiologic loads (Humphrey, 2002)).

To account for the stability afforded by the carotid sheath that surrounds the carotid artery *in vivo*, perivascular tissue was modelled by adding a linear elastic material layer around and attached to the outermost vessel layer with an elastic modulus of 28 Pa and Poisson's ratio of 0.05 (highly compressible). The thickness and material properties were optimized to minimize the impact on the vessel wall's dilatation at 80 mmHg and 120 mmHg pressurisation.

Blood was modelled as an incompressible non-Newtonian fluid using the Carreau-Yasuda model, (Johnston et al., 2004) given by

$$\eta = \eta_\infty + (\eta_0 - \eta_\infty)(1 + (\lambda \dot{\gamma})^\alpha)^{\frac{n-1}{\alpha}} \tag{2}$$

where parameters were chosen to be $\eta_\infty = 55$ Pa.s, $\eta_0 = 3.45$ Pa.s, $\lambda = 3.313$, $n = 0.3568$, $\alpha = 2$. Blood density was also prescribed as 1050 kg/m^3.

2.3. Finite element modelling of artery pre-stresses

Multiple studies (Debes and Fung, 1995; Guo et al., 2005; Matsumoto and Hayashi, 1996; Otoguro et al., 2015; Taber, 2001) indicate that the *in vivo* arterial wall in diastole is exposed to a circumferential residual
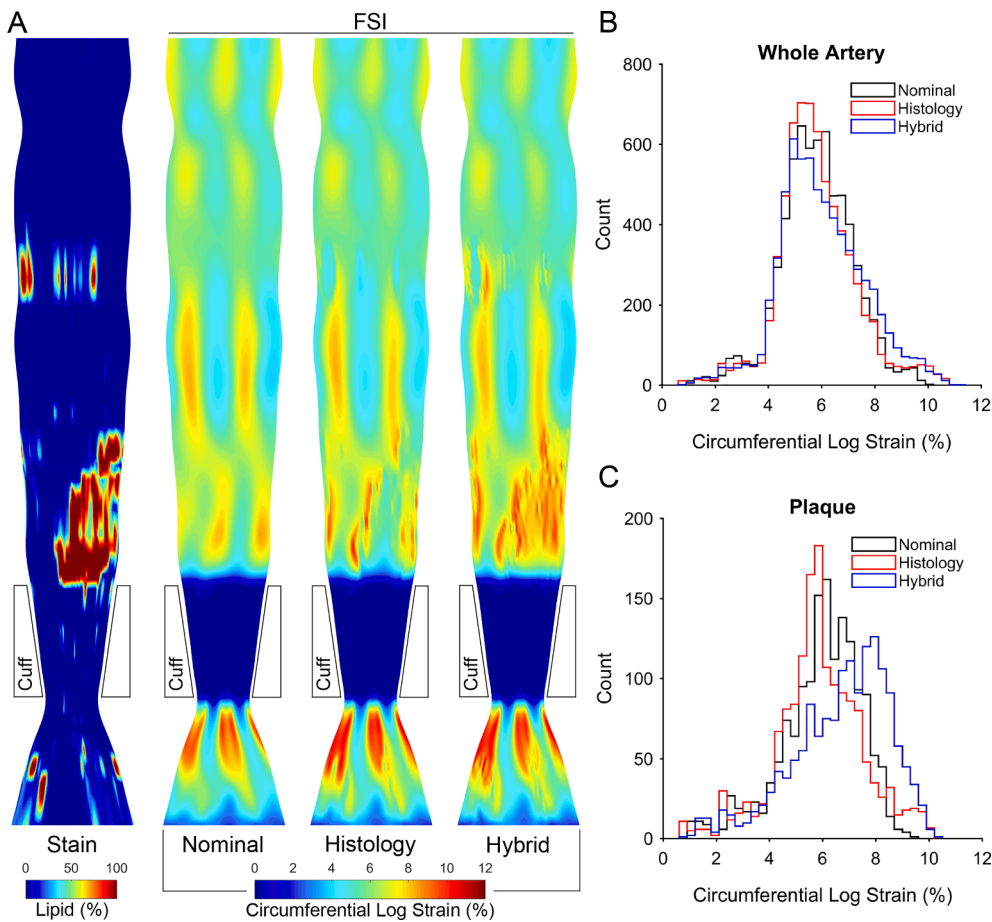
Fig. 4. Cyclic circumferential logarithmic strain (%) from FSI simulations of the Nominal Model, Histology Model, and Hybrid Model. (A) 2D projections of each metric from the 3D artery from near the aortic arch (top) to just before the carotid bifurcation (bottom) showing the distribution of oil red O (lipid) staining and circumferential logarithmic strain (%) at the inner lining of the artery (endothelial strain) from the FSI simulations. (B and C) Histograms of the number of elements (count) for each increment of circumferential logarithmic strain (0.3%) in FSI (B) over the whole artery (excluding the cuff area) and (C) only in regions of lipid deposition (plaque) for each of the three models.

stress (i.e., stress that exists in the absence of applied loads) and an axial prestress due to elongation in situ (Cardamone et al., 2009; Guo et al., 2005; Maes et al., 2019; Taber, 2001). In addition, the *in vivo* artery is prestressed by end-diastolic blood pressure. To account for this initial stress state, sequential solids-only simulations were run in Abaqus (v6.14), where the final stress field from each simulation was used as the initial condition for the next simulation, as follows. First, circumferential residual stress was determined by using a straightened-equivalent artery model with a circumferential opening of 92° (Hansen et al., 2013) that was closed through application of a rotation to connect one side of the opening to the other, which was held fixed. Second, axial prestress was determined by applying a 40 kPa axial load (Gleason et al., 2007). The load was applied over 10 steps using the Backward Incremental method (de Putter et al., 2007; Speelman et al., 2009), which utilises the *in vivo* geometry from micro-CT as the initial geometry for each simulation, with the computed resultant stress field from the prior step providing the model stress for initialisation of the subsequent step. Third, the blood pressure prestress was obtained by applying 80 mmHg over 12 steps, again using the Backward Incremental method. All simulations in the pressurisation steps were constrained axially at both ends. The computed stress field from the final simulation (referred to simply as "prestresses" or the prestressed configuration) was used as the initial stress state of the FSI model.

2.4. FSI modelling

The FSI simulations were performed with Abaqus/Standard 6.14 and Abaqus/CFD 6.14 modules (Dassault Systems) as part of a co-simulation based on the Arbitrary Lagrangian-Eulerian (ALE) method. In this approach, the mesh is conserved between the fluid-solid interface at the inner surface of the vessel wall, the pressure and the shear stresses are passed from the blood flow side of this interface to the vessel wall, and the wall displacement and actual diameters are passed from the vessel side to the fluid domain simulation.

For the control vessel FSI model, the nominal vessel thickness was assumed to be a constant value of 50 μm and the prestresses for this model were computed using the vessel geometry with the aforementioned nominal thickness. For the instrumented or cuffed vessel, three FSI models were formulated as follows:

A) Nominal Model   Nominal thickness and homogenous wall material FSI model with the prestresses.
B) Histology Model   Histology-based wall thickness FSI model with heterogeneous wall material properties based on the degree of lipid staining initialised before computing the prestresses.
C) Hybrid Model   Histology-based wall thickness FSI model with heterogeneous wall material properties and prestresses obtained from the Histology Model (B), but with homogeneous material properties. This aims to represent the prestresses that largely develop during normal (healthy) vessel wall growth, prior to the development of atherosclerosis due to cuff placement. In this model, prestresses calculated in the regions of lipid deposition were set to zero.

2.4.1. Boundary conditions

A blood velocity waveform was measured by Doppler ultrasound (Vevo 770) for each carotid artery and applied to the inlet of each model with a prescribed parabolic profile. An outlet boundary model (Pahlevan et al., 2011) was added to simulate the compliance and resistance of the downstream vasculature. The compliance of 2.5E−14 m^4s^2/kg was computed using previously published values for compliance and
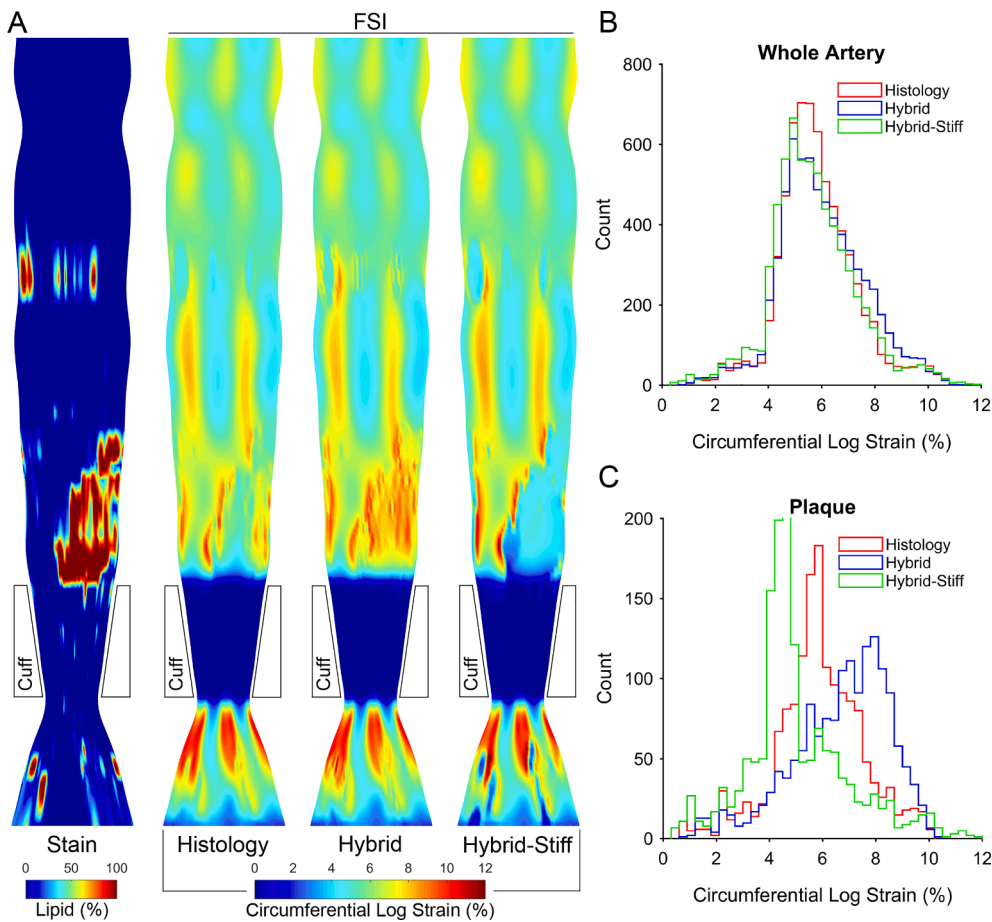
Fig. 5. Cyclic circumferential logarithmic strain (%) from FSI simulations of the Histology Model, Hybrid Model, and Hybrid-Stiff Model. (A) 2D projections of each metric from the 3D artery from near the aortic arch (top) to just before the carotid bifurcation (bottom) showing the distribution of oil red O (lipid) staining and circumferential logarithmic strain (%) at the inner lining of the artery (endothelial strain) from the FSI simulations. (B and C) Histograms of the number of elements (count) for each increment of circumferential logarithmic strain (0.3%) in FSI (B) over the whole artery (excluding the cuff area) and (C) only in regions of lipid deposition (plaque) for each of the three models.

resistance (Aslanidou et al., 2016). Resistance was optimised to achieve 80 mmHg diastolic pressure. All additional boundary conditions are given in Table S1 (Appendix A).

2.5. Shear and strain metrics

The TAWSS was calculated for each element on the lumen wall over one cardiac cycle (Pedrigi et al., 2016). In addition, endothelial strain was reported based on logarithmic strain obtained from the FSI models for the innermost elements of the artery. The strain field in the FSI model stems from a combination of strains developed from the prestresses and the pulsatile pressure over the cardiac cycle (Fig. 2). Since endothelial cells have a short half-life (20–40 days), their stress-free length is reasonably assumed to be at diastole. In addition, endothelial cell function is likely most impacted by the circumferential strain of the artery because this direction experiences the largest change in strain over the cardiac cycle (Pedrigi et al., 2017). Thus, herein, we focused on cyclic circumferential strain, computed as the difference between systole and diastole.

3. Results

The control vessel FSI simulations produced pressures of 82/110 mmHg and a peak physiologic dilatation of 11.6% (Fig. 3). Time-averaged wall shear stress maps for all models are given in Fig. S2 (Appendix A).

3.1. A novel Hybrid FSI Model predicts altered strain in local regions of plaque

An important aim in this study was to develop FSI models with all

relevant prestresses which captured local heterogeneities in the strain field that resulted from altered plaque properties. We began with the Histology Model of the instrumented artery (for definition see above), where softer material properties in regions of lipid deposition were initialized *before* computing prestresses. This model predicted a median circumferential strain in the plaque regions of 5.8% (Fig. 4C). Interestingly, this was slightly *less* than the 6.1% within the same spatial locations of the Nominal Model, which does not consider softer properties due to lipid deposition. Since the FSI model should predict higher strains in local regions of the atherosclerotic artery that are more compliant due to the presence of lipids, we developed a hybrid approach where prestresses were computed using normal material properties over the whole artery and set to zero in regions of lipid deposition. The Hybrid Model exhibited the expected increased compliance in the plaque regions compared to the other models with a median circumferential strain of 7.0% (Fig. 4C). A similar trend was observed with the radial strain, whereby the Hybrid Model exhibited the largest (compressive) radial strain in regions of lipid deposition of −7.0% compared to −5.2% and −5.7% in the Histology Model and Nominal Model, respectively (Fig. S3). Strain in the axial direction showed little change over the cardiac cycle (Fig. S4, Appendix A).

To further demonstrate the robustness of the Hybrid Model, we also evaluated whether it could predict realistic changes in artery wall strain with *increased* stiffness of the plaque regions, such as occurs with a fibrous cap atheroma. This Hybrid-Stiff Model was simulated with an arbitrary 10-fold increase in stiffness of the lipid regions. It predicted the expected lower circumferential strain within these regions of 4.6% compared to both the softer properties of the Hybrid Model and normal properties of the Nominal model (Fig. 5). These results demonstrate that our hybrid approach is capable of capturing changes in local stiffness in diseased arteries.
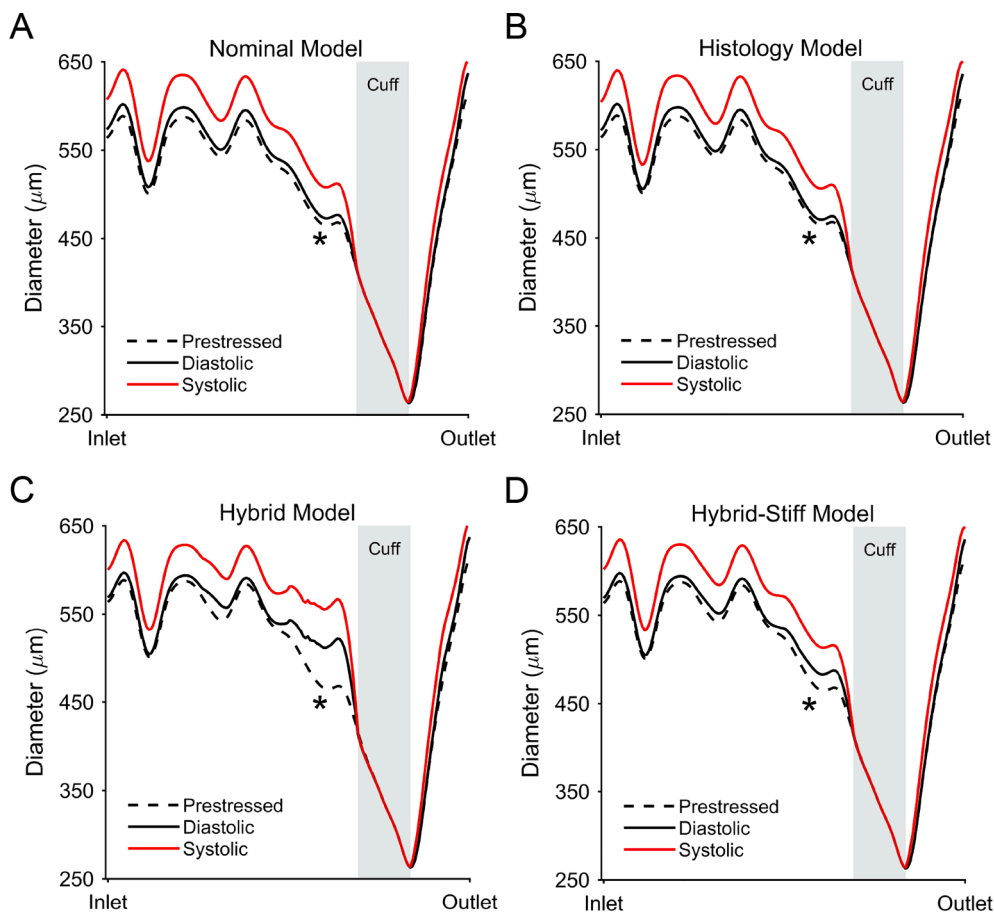
Fig. 6. Diameter of the instrumented carotid artery from the inlet (near the aortic arch) to the outlet (near the carotid bifurcation) for the (A) Nominal Model, (B) Histology Model, (C) Hybrid Model, and (D) Hybrid-Stiff Model. Region of cuff placement is lightly greyed. *Indicates the center of the upstream plaque, where the Hybrid Model exhibited increased dilatation compared to the other models due to the softer lipid properties and method of incorporating the prestresses. Because this method involved setting the final prestress in the lipid regions to zero, this increased dilatation of the Hybrid Model was seen both at diastole (compared to the prestressed configuration) and over the cardiac cycle.

To better understand the resultant circumferential strains exhibited by the different FSI models, we also evaluated diameter over the length of the instrumented artery in the prestressed configuration (before starting the FSI simulation), diastole, and systole. As expected, we found that, the diameter of the artery after computing the prestresses in the Nominal Model and Histology Model was nearly identical to that in the FSI simulations during diastole, which results from using the Backward Incremental method to compute prestresses. In contrast, it was significantly larger in the hybrid models in regions of lipid deposition, where prestresses were set to zero, at both diastole and systole (Fig. 6). As a result, circumferential strain at systole computed relative to the prestressed configuration was 30.5% in the Hybrid Model and 11.8% in the Hybrid-Stiff Model, compared to 7.1% and 7.7% in the Histology Model and Nominal Model, respectively.

3.2. The Hybrid Model predicts lower TAWSS than the other FSI models and CFD

The Nominal Model with uniform material properties predicted a median difference in TAWSS compared to the corresponding CFD simulation over the whole vessel (outside of the cuff) of −11.5% (Fig. 7A and B). To our surprise, the Histology Model predicted a TAWSS profile over the whole vessel that was nearly identical to the Nominal Model with a median difference in TAWSS compared to CFD of −11.2%. Correspondingly, the median difference in TAWSS between each of these FSI models and CFD within only the plaque regions was similar for the Histology Model compared to the Nominal Model with values of −11.3% and −12.0%, respectively (Fig. 7C). In contrast, the Hybrid Model resulted in a much larger median difference in TAWSS from CFD in the plaque regions of −23.8%, but was similar over the artery as a whole with a difference of −11.4% (Fig. 7A–C). These results

demonstrate that predictions of endothelial shear stress are not only lower in an FSI model, in general, but, in the case of the Hybrid Model, are also more heterogeneous due to the effect of altered properties in regions of plaque.

4. Discussion

This paper presents the development of FSI models of an atherosclerotic with local tissue properties and normal carotid artery from an ApoE$^{-/-}$ mouse. We found that the normal artery model predicted physiologically accurate values for blood pressure, vessel dilatation, and flow, comparable to previously reported measurements in mice (De Wilde et al., 2016a, 2016b). To our knowledge, only one other group has developed an FSI model of the mouse carotid artery (De Wilde et al., 2016a, 2016b, 2016c), but this work had a lesser emphasis on the endothelial wall mechanics, including no consideration of altered wall properties with plaque development. The focus of our paper was the development of an FSI model with altered properties in regions of lipid deposition to evaluate how different modelling assumptions related to the incorporation of "prestresses" within the artery wall (i.e., circumferential residual stress and prestresses due to axial elongation and diastolic blood pressure) affect prediction of endothelial shear stress and strain. Since murine atherosclerosis is often associated with lipid-rich plaques, probably due to the extremely high cholesterol levels that are achieved through genetic modification and diet to accelerate atherosclerosis (Tang et al., 2005; Tracqui et al., 2011), we focused plaque properties solely on the presence of softer lipids within local regions of the Histology Model and hybrid models, which were assigned based on co-registered, serially-collected oil red O-stained histology sections (an approach called 3-D histology) (Segers et al., 2007).

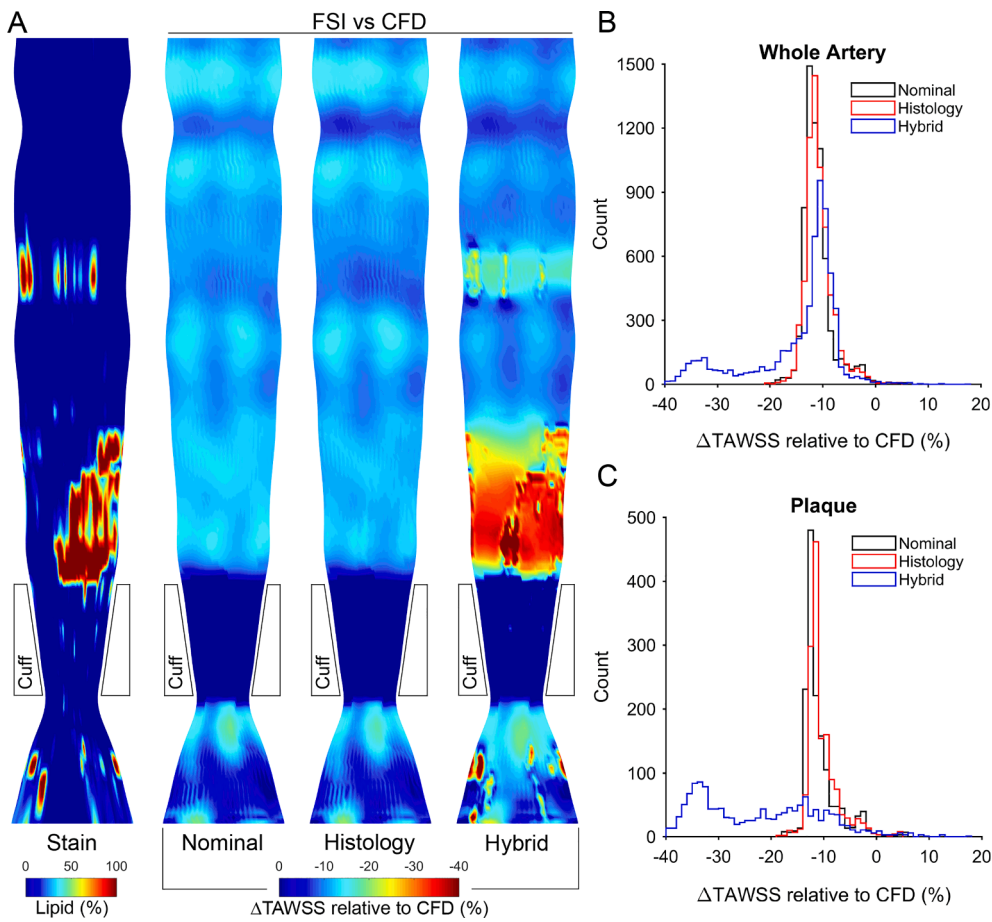We found that incorporating these local changes in wall properties

Fig. 7. The percent difference in TAWSS (ΔTAWSS) of FSI relative to CFD simulations for the Nominal Model, Histology Model, and Hybrid Model. (A) 2D projections of each metric on the artery from near the aortic arch (top) to just before the carotid bifurcation (bottom) showing the distribution of oil red O (lipid) staining and ΔTAWSS of FSI relative to the same model in CFD. (B and C) Histograms of the number of elements (count) for each increment of ΔTAWSS (1%) in FSI (B) over the whole artery (excluding the cuff area) and (C) only in regions of lipid deposition (plaque) for each of the three models.

prior to the calculation of prestresses via the Histology Model led to almost no difference in either circumferential strain or TAWSS as compared to the Nominal Model with normal properties, even in plaque regions. This was due to the formation of higher strains within the more compliant regions of lipid deposition in the Histology Model that caused a stiffening effect from the nonlinear material properties. As a result, the lipid regions at the start of the FSI simulation had similar stress and stiffness to the surrounding normal wall (Fig. S5, Appendix A). To avoid this problem, the Hybrid Model calculated the prestresses using normal wall properties over the entire vessel (even in plaque regions) and only incorporated them into the non-diseased regions, with regions of lipid deposition assumed to be stress-free at the start of the FSI simulation. This model predicted the expected increased compliance and decreased TAWSS on the endothelium overlaying the plaques. Thus, we found that plaque properties should be introduced into an FSI model after the calculation of prestresses. This is significant because it aligns with other studies that have shown residual stress and prestresses to depend primarily on elastin, not collagen, which is deposited during normal (healthy) vessel wall growth and has a half-life comparable to the lifespan of the organism (Cardamone et al., 2009), so exists prior to the development of atherosclerosis.

4.1. Limitations

There are three primary limitations to consider in this study. First, we performed FSI modelling on the atherosclerotic and non-atherosclerotic carotid arteries from only one mouse. Since the purpose of this study was to describe the development of the FSI models and evaluate how different assumptions related to the incorporation of prestresses affect prediction of endothelial shear stress and strain, not to demonstrate connections between mechanical metrics and the

associated pathobiology, one mouse is sufficient because these assumptions are independent of the specific arteries used (i.e., geometries, mechanical properties and blood velocities). Second, a common limitation of murine arterial wall modelling is the lack of local temporal pressure measurements. Pressure measurements are difficult to obtain in mice due to their small size. Tail pressure measurements are available, but these are not sufficiently accurate or acquired in the area of interest, so are not considered suitable replacements for carotid artery pressure (Zhao et al., 2011). Other invasive methods require sacrificing the animal. We opted for a boundary model based on both measured and estimated compliance and resistance values for downstream mouse vasculature. This outlet model results in a vessel distension that compares well with M-mode measurements (Fig. 3B). Third, mechanical properties used for the artery wall were based on a fit of the isotropic Ogden model to previously reported experimental inflation data from wild-type mice (Eberth et al., 2009). We justified the use of an isotropic model based on the small degree of anisotropy between the mean axial and circumferential mechanical behaviour curves obtained from the defined constitutive model for several mice in this previous study.

4.2. Conclusions

This study describes the influence of assumptions in the development of FSI models of locally diseased blood vessels on the prediction of endothelial shear stress and strain. We found that prestresses should be computed using normal material properties and assigned only to non-diseased regions of the artery wall; plaque regions should have zero stress at the start of the FSI simulation. Using this approach, we also found that FSI predicted significantly lower endothelial shear stress compared to CFD and that this difference was even greater in regions of lipid deposition. This resulted in significant heterogeneity of endothelial

shear stress in the atherosclerotic artery due to variations in stiffness and, in turn, wall strain. Since such variations cannot be captured by CFD, this finding demonstrates that FSI more accurately predicts shear stress in atherosclerotic arteries, which may increase predictability of associated biomarkers of plaque development. Further studies are needed with a larger cohort of mice to address improved prediction of plaque development using FSI compared to CFD.

Declaration of Competing Interest

The authors declare that they have no known competing financial interests or personal relationships that could have appeared to influence the work reported in this paper.

Acknowledgements

Appendix A. Supplementary material

Supplementary data to this article can be found online at https://doi.org/10.1016/j.jbiomech.2021.110720.

References

Alberts-Grill, N., Denning, T.L., Rezvan, A., Jo, H., 2013. The role of the vascular dendritic cell network in atherosclerosis. Am. J. Physiol. Cell Physiol. 305, C1–C21. https://doi.org/10.1152/ajpcell.00017.2013.

Aslanidou, L., Trachet, B., Reymond, P., Fraga-Silva, R.A., Segers, P., Stergiopulos, N., 2016. A 1D model of the arterial circulation in mice. ALTEX 33, 13–28. https://doi.org/10.14573/altex.1507071.

Cardamone, L., Valentin, A., Eberth, J.F., Humphrey, J.D., 2009. Origin of axial prestretch and residual stress in arteries. Biomech. Model. Mechanobiol. 8, 431–446. https://doi.org/10.1007/s10237-008-0146-x.

Cheng, C., Tempel, D., van Haperen, R., van der Baan, A., Grosveld, F., Daemen, M.J., Krams, R., de Crom, R., 2006. Atherosclerotic lesion size and vulnerability are determined by patterns of fluid shear stress. Circulation 113, 2744–2753. https://doi.org/10.1161/CIRCULATIONAHA.105.590018.

Chester, A.H., El-Hamamsy, I., Butcher, J.T., Latif, N., Bertazzo, S., Yacoub, M.H., 2014. The living aortic valve: from molecules to function. Glob. Cardiol. Sci. Pract. 2014, 52–77. https://doi.org/10.5339/gcsp.2014.11.

Chistiakov, D.A., Revin, V.V., Sobenin, I.A., Orekhov, A.N., Bobryshev, Y.V., 2015. Vascular endothelium: functioning in norm, changes in atherosclerosis and current dietary approaches to improve endothelial function. Mini Rev. Med. Chem.

de Putter, S., Wolters, B.J., Rutten, M.C., Breeuwer, M., Gerritsen, F.A., van de Vosse, F. N., 2007. Patient-specific initial wall stress in abdominal aortic aneurysms with a backward incremental method. J. Biomech. 40, 1081–1090. https://doi.org/10.1016/j.jbiomech.2006.04.019.

De Wilde, D., Trachet, B., De Meyer, G., Segers, P., 2016a. The influence of anesthesia and fluid-structure interaction on simulated shear stress patterns in the carotid bifurcation of mice. J. Biomech. 49, 2741–2747. https://doi.org/10.1016/j.jbiomech.2016.06.010.

De Wilde, D., Trachet, B., De Meyer, G.R.Y., Segers, P., 2016b. Shear stress metrics and their relation to atherosclerosis: an in vivo follow-up study in atherosclerotic mice. Ann. Biomed. Eng. 44, 2327–2338. https://doi.org/10.1007/s10439-015-1540-z.

De Wilde, D., Trachet, B., Debusschere, N., Iannaccone, F., Swillens, A., Degroote, J., Vierendeels, J., De Meyer, G.R.Y., Segers, P., 2016c. Assessment of shear stress related parameters in the carotid bifurcation using mouse-specific FSI simulations. J. Biomech. 49, 2135–2142. https://doi.org/10.1016/j.jbiomech.2015.11.048.

Debes, J.C., Fung, Y.C., 1995. Biaxial mechanics of excised canine pulmonary arteries. Am. J. Physiol. 269, H433–H442. https://doi.org/10.1152/ajpheart.1995.269.2.H433.

Eberth, J.F., Taucer, A.I., Wilson, E., Humphrey, J.D., 2009. Mechanics of carotid arteries in a mouse model of Marfan Syndrome. Ann. Biomed. Eng. 37, 1093–1104. https://doi.org/10.1007/s10439-009-9686-1.

Fung, Y.C., 1991. What are the residual stresses doing in our blood vessels? Ann. Biomed. Eng. 19, 237–249.

Gleason, R.L., Wilson, E., Humphrey, J.D., 2007. Biaxial biomechanical adaptations of mouse carotid arteries cultured at altered axial extension. J. Biomech. 40, 766–776. https://doi.org/10.1016/j.jbiomech.2006.03.018.

Guo, X., Lu, X., Kassab, G.S., 2005. Transmural strain distribution in the blood vessel wall. Am. J. Physiol. Heart Circ. Physiol. 288, H881–H886. https://doi.org/10.1152/ajpheart.00607.2004.

Hansen, L., Parker, I., Sutliff, R.L., Platt, M.O., Gleason Jr., R.L., 2013. Endothelial dysfunction, arterial stiffening, and intima-media thickening in large arteries from HIV-1 transgenic mice. Ann. Biomed. Eng. 41, 682–693. https://doi.org/10.1007/s10439-012-0702-5.

Humphrey, J.D., 2002. Cardiovascular Solid Mechanics: Cells, Tissues, and Organs. Springer-Verlag, New York.

Johnston, B.M., Johnston, P.R., Corney, S., Kilpatrick, D., 2004. Non-Newtonian blood flow in human right coronary arteries: steady state simulations. J. Biomech. 37, 709–720. https://doi.org/10.1016/j.jbiomech.2003.09.016.

Kobielarz, M., Kozun, M., Gasior-Glogowska, M., Chwilkowska, A., 2020. Mechanical and structural properties of different types of human aortic atherosclerotic plaques. J. Mech. Behav. Biomed. Mater. 109, 103837 https://doi.org/10.1016/j.jmbbm.2020.103837.

Krams, R., Verheye, S., van Damme, L.C., Tempel, D., Mousavi Gourabi, B., Boersma, E., Kockx, M.M., Knaapen, M.W., Strijder, C., van Langenhove, G., Pasterkamp, G., van der Steen, A.F., Serruys, P.W., 2005. In vivo temperature heterogeneity is associated with plaque regions of increased MMP-9 activity. Eur. Heart J. 26, 2200–2205. https://doi.org/10.1093/eurheartj/ehi461.

Kwak, B.R., Back, M., Bochaton-Piallat, M.L., Caligiuri, G., Daemen, M.J., Davies, P.F., Hoefer, I.E., Holvoet, P., Jo, H., Krams, R., Lehoux, S., Monaco, C., Steffens, S., Virmani, R., Weber, C., Wentzel, J.J., Evans, P.C., 2014. Biomechanical factors in atherosclerosis: mechanisms and clinical implications. Eur. Heart J. 35, 3013-3020, 3020a-3020d. https://doi.org/10.1093/eurheartj/ehu353.

Liu, X.M., Peyton, K.J., Durante, W., 2013. Physiological cyclic strain promotes endothelial cell survival via the induction of heme oxygenase-1. Am. J. Physiol. Heart Circ. Physiol. 304, H1634–H1643. https://doi.org/10.1152/ajpheart.00872.2012.

Maes, L., Fehervary, H., Vastmans, J., Mousavi, S.J., Avril, S., Famaey, N., 2019. Constrained mixture modeling affects material parameter identification from planar biaxial tests. J. Mech. Behav. Biomed. Mater. 95, 124–135. https://doi.org/10.1016/j.jmbbm.2019.03.029.

Matsumoto, T., Hayashi, K., 1996. Stress and strain distribution in hypertensive and normotensive rat aorta considering residual strain. J. Biomech. Eng. 118, 62–73. https://doi.org/10.1115/1.2795947.

Morbiducci, U., Kok, A.M., Kwak, B.R., Stone, P.H., Steinman, D.A., Wentzel, J.J., 2016. Atherosclerosis at arterial bifurcations: evidence for the role of haemodynamics and geometry. Thromb. Haemost. 115, 484–492. https://doi.org/10.1160/TH15-07-0597.

Otoguro, S., Hayashi, Y., Miura, T., Uehara, N., Utsumi, S., Onuki, Y., Obata, Y., Takayama, K., 2015. Numerical investigation of the residual stress distribution of flat-faced and convexly curved tablets using the finite element method. Chem. Pharm. Bull. (Tokyo) 63, 890–900. https://doi.org/10.1248/cpb.c15-00481.

Pahlevan, N.M., Amlani, F., Hossein Gorji, M., Hussain, F., Gharib, M., 2011. A physiologically relevant, simple outflow boundary model for truncated vasculature. Ann. Biomed. Eng. 39, 1470–1481. https://doi.org/10.1007/s10439-011-0246-0.

Pedrigi, R.M., de Silva, R., Bovens, S.M., Mehta, V.V., Petretto, E., Krams, R., 2014. Thin-cap fibroatheroma rupture is associated with a fine interplay of shear and wall stress. Arterioscler. Thromb. Vasc. Biol. 34, 2224–2231. https://doi.org/10.1161/ATVBAHA.114.303426.

Pedrigi, R.M., Mehta, V.V., Bovens, S.M., Mohri, Z., Poulsen, C.B., Gsell, W., Tremoleda, J.L., Towhidi, L., de Silva, R., Petretto, E., Krams, R., 2016. Influence of shear stress magnitude and direction on atherosclerotic plaque composition. R. Soc. Open Sci. 3, 160588 https://doi.org/10.1098/rsos.160588.

Pedrigi, R.M., Papadimitriou, K.I., Kondiboyina, A., Sidhu, S., Chau, J., Patel, M.B., Baeriswyl, D.C., Drakakis, E.M., Krams, R., 2017. Disturbed cyclical stretch of endothelial cells promotes nuclear expression of the pro-atherogenic transcription factor NF-kappaB. Ann. Biomed. Eng. 45, 898–909. https://doi.org/10.1007/s10439-016-1750-z.

Pedrigi, R.M., Poulsen, C.B., Mehta, V.V., Ramsing Holm, N., Pareek, N., Post, A.L., Kilic, I.D., Banya, W.A., Dall'Ara, G., Mattesini, A., Bjorklund, M.M., Andersen, N.P., Grondal, A.K., Petretto, E., Foin, N., Davies, J.E., Di Mario, C., Fog Bentzon, J., Erik Botker, H., Falk, E., Krams, R., de Silva, R., 2015. Inducing persistent flow disturbances accelerates atherogenesis and promotes thin cap fibroatheroma development in D374Y-PCSK9 hypercholesterolemic minipigs. Circulation 132, 1003–1012. https://doi.org/10.1161/CIRCULATIONAHA.115.016270.

Peters, A.S., Brunner, G., Krieg, T., Eckes, B., 2015. Cyclic mechanical strain induces TGFbeta1-signalling in dermal fibroblasts embedded in a 3D collagen lattice. Arch. Dermatol. Res. 307, 191–197. https://doi.org/10.1007/s00403-014-1514-2.

Segers, D., Helderman, F., Cheng, C., van Damme, L.C., Tempel, D., Boersma, E., Serruys, P.W., de Crom, R., van der Steen, A.F., Holvoet, P., Krams, R., 2007. Gelatinolytic activity in atherosclerotic plaques is highly localized and is associated with both macrophages and smooth muscle cells in vivo. Circulation 115, 609–616. https://doi.org/10.1161/CIRCULATIONAHA.106.636415.

Speelman, L., Bosboom, E.M., Schurink, G.W., Buth, J., Breeuwer, M., Jacobs, M.J., van de Vosse, F.N., 2009. Initial stress and nonlinear material behavior in patient-specific AAA wall stress analysis. J. Biomech. 42, 1713–1719. https://doi.org/10.1016/j.jbiomech.2009.04.020.

Stone, P.H., Maehara, A., Coskun, A.U., Maynard, C.C., Zaromytidou, M., Siasos, G., Andreou, I., Fotiadis, D., Stefanou, K., Papafaklis, M., Michalis, L., Lansky, A.J., Mintz, G.S., Serruys, P.W., Feldman, C.L., Stone, G.W., 2018. Role of low endothelial shear stress and plaque characteristics in the prediction of nonculprit major adverse

cardiac events: the PROSPECT study. JACC Cardiovasc Imaging 11, 462–471. https://doi.org/10.1016/j.jcmg.2017.01.031.

Taber, L.A., 1995. Biomechanics of growth, remodeling, and morphogenesis. Appl. Mech. Rev. 48, 487–545. https://doi.org/10.1115/1.3005109.

Taber, L.A., 2001. Stress-modulated growth, residual stress, and vascular heterogeneity. J. Biomech. Eng. 123, 528–535.

Tang, D., Yang, C., Zheng, J., Woodard, P.K., Saffitz, J.E., Sicard, G.A., Pilgram, T.K., Yuan, C., 2005. Quantifying effects of plaque structure and material properties on stress distributions in human atherosclerotic plaques using 3D FSI models. J. Biomech. Eng. 127, 1185–1194. https://doi.org/10.1115/1.2073668.

Tian, J., Ren, X., Uemura, S., Dauerman, H., Prasad, A., Toma, C., Jia, H., Abtahian, F., Vergallo, R., Hu, S., McNulty, I., Lee, H., Lee, S., Yu, B., Jang, I.K., 2014. Spatial heterogeneity of neoatherosclerosis and its relationship with neovascularization and adjacent plaque characteristics: optical coherence tomography study. Am. Heart J. 167 (884–892), e882 https://doi.org/10.1016/j.ahj.2014.03.013.

Trachet, B., Bols, J., Degroote, J., Verhegghe, B., Stergiopulos, N., Vierendeels, J., Segers, P., 2015. An animal-specific FSI model of the abdominal aorta in anesthetized mice. Ann. Biomed. Eng. 43, 1298–1309. https://doi.org/10.1007/s10439-015-1310-y.

Tracqui, P., Broisat, A., Toczek, J., Mesnier, N., Ohayon, J., Riou, L., 2011. Mapping elasticity moduli of atherosclerotic plaque in situ via atomic force microscopy. J. Struct. Biol. 174, 115–123. https://doi.org/10.1016/j.jsb.2011.01.010.

Trogan, E., Choudhury, R.P., Dansky, H.M., Rong, J.X., Breslow, J.L., Fisher, E.A., 2002. Laser capture microdissection analysis of gene expression in macrophages from atherosclerotic lesions of apolipoprotein E-deficient mice. Proc. Natl. Acad. Sci. USA 99, 2234–2239. https://doi.org/10.1073/pnas.042683999.

Yurdagul Jr., A., Finney, A.C., Woolard, M.D., Orr, A.W., 2016. The arterial microenvironment: the where and why of atherosclerosis. Biochem. J. 473, 1281–1295. https://doi.org/10.1042/BJ20150844.

Zhao, X., Ho, D., Gao, S., Hong, C., Vatner, D.E., Vatner, S.F., 2011. Arterial pressure monitoring in mice. Curr. Protoc. Mouse Biol. 1, 105–122. https://doi.org/10.1002/9780470942390.mo100149.